Surface premelting of Cu(110)

R. N. Barnett and Uzi Landman
School of Physics, Georgia Institute of Technology, Atlanta, Georgia 30332
(Received 19 February 1991)

Disordering and melting of the surface of Cu(110) are investigated using molecular-dynamics simulations, in which the embedded-atom theory is used to describe the energetics and interatomic interactions. In addition, the bulk melting temperature and the properties of the crystal-to-melt interface at coexistence are studied. The surface region of the Cu(110) starts to disorder, via the generation of vacancies accompanied by the formation of an adlayer, at a temperature of about 900 K. At a temperature of $\simeq 1200$ K (i.e., about 80 K below bulk melting), the development of a quasiliquid region, exhibiting liquidlike energetic, structural, and transport properties, is observed. Analysis of the results, motivated by Landau-Ginzburg (mean-field) theories of surface melting, shows that the thickness of the quasiliquid layer increases logarithmically as the temperature approaches the melting point, with a correlation length of 4.3 Å.

I. INTRODUCTION

The suggestion that melting nucleates at the surface of the solid and then propagates inward and the idea that the surface of a solid may become liquid at a temperature below the (nominal) bulk melting point T_m dates back over a century.[1] While numerous attempts to detect surface-initiated melting phenomena have been made,[2-7] it is only recently that direct observations of surface melting have been made on a microscopic level and employing atomically clean, well-characterized surfaces. The first direct observations[8-10] were made using Rutherford backscattering, in conjunction with shadowing and blocking. Since then, other techniques have been employed, such as calorimetry,[11-16] ellipsometry,[17,18] electron diffraction[18-23] and microscopy,[24] neutron[25] and x-ray diffraction,[26,27] quasielastic neutron[28] and helium scattering,[29,30] and even visual inspection with the naked eye.[31,32]

Surface melting can be viewed as the wetting of the solid-gas interface by the liquid (or quasiliquid, see the following) upon approaching the triple point.[2-4] We emphasize that from this perspective we treat melting as a thermal equilibrium phenomenon (devoid of kinetic effects) distinguished from melting of a crystal surface following irradiation (by a short photon pulse or electron beam as in laser and electron surface annealing experiments), which is a nonequilibrium phenomenon. We note, however, that the surface melt layer at the initial stages of the process should be regarded as a quasiliquid exhibiting structural, dynamical, and transport properties that are intermediate between those of the solid and the bulk liquid. It is the formation of the thin quasiliquid layer, whose thickness grows as the temperature approaches T_m, which one terms appropriately as surface premelting.[2,3]

One of the interesting results of the experimental studies of surface melting is the crystalline face anisotropy of the phenomenon.[33] Thus, while the open faces of certain fcc crystals [Pb(110), Al(110)] exhibit surface melting as defined above,[3,20,33] the phenomenon is not observed for the close-packed surfaces[3,34] [Pb(111) and Al(111)]. These observations have been rationalized using a phenomenological Landau-Ginzburg formulation,[2,3,35-38] leading to a "surface melting condition," which relates the interfacial free energies of the three phases, γ_{sv}, γ_{lv}, and γ_{sl}, corresponding to solid vapor, liquid-vapor, and solid-liquid equilibrium, respectively. The condition[2,3]

$$\gamma_{sv}^{(hkl)}-\gamma_{lv}^{(hkl)}-\gamma_{sl}^{(hkl)}\equiv\Delta\gamma^{(hkl)}>0 \tag{1}$$

expresses the energy balance when a dry solid surface is replaced by one wetted by a liquid layer. The larger $\Delta\gamma^{(hkl)}$ is, the greater is the free-energy gain and thus the tendency for surface premelting (the dependence of the γ's on crystalline face is explicitly noted). According to this condition the surface will remain dry (i.e., no premelting) when $\Delta\gamma<0$. We remark[3] that strictly speaking the interfacial free energies in Eq. (1) are not necessarily the same as the equilibrium values for infinitely thick liquid films (consequently the crystal-face dependence of $\gamma_{sl}^{(hkl)}$ and $\gamma_{lv}^{(hkl)}$ which refers to the quasiliquid as discussed above). However, as argued previously,[3] out-of-equilibrium values can be estimated by extrapolation of known (empirical or semiempirical) equilibrium values. This criterion has been used[3] to explain the results for Pb(110), where good estimates of the interfacial free energies are available.

Most theoretical approaches to surface melting are of thermodynamical[4,39-43] and/or phenomenological nature, including lattice dynamics and stability analysis,[44-47] lattice-gas models (employing mean-field[48] and the cluster variation method),[49] and Landau theory.[2,3,35-38] Microscopic descriptions of surface disordering and melting phenomena emerged from computer molecular-dynamics (MD) simulations which until recently[50-52] employed[53-57] simple pairwise interatomic interactions in the form of Lennard-Jones potentials,

which are appropriate for the description of rare-gas solids and liquids, but are known to be inadequate for metals.

In our previous studies we have investigated the melting of Al(110) (Ref. 50) and Ni(110),[51] using many-body interaction potential derived from the effective-medium[58] and embedded-atom[59,60] (EAM) theories, respectively. While a clear premelting tendency at a temperature significantly below the melting point T_m was observed from the MD simulations for Al(110) [and the lack thereof for Al(111)], the results[51] obtained for Ni(110) may be summarized as follows.

(i) At low temperatures ($T \lesssim 1450$ K) the response of the system to increase in temperature can be explained in terms of anharmonic vibrational effects, and for these temperatures there is no indication for loss of long-range order due to defect formation and/or significant atomic diffusion. Atoms in the surface region of the material vibrate with larger mean-square vibrational amplitudes than those in deeper layers in the material, and their displacements are largest in the $[1\bar{1}0]$ direction (along the atomic rows) reflecting the crystallographical anisotropy of the surface. Furthermore analysis of the temperature behavior of the structure factors versus temperature indicates that the anharmonicity of the vibrations in the [001] direction (across the atomic rows) is larger than that along the $[1\bar{1}0]$ and the [110] directions.

(ii) The onset of disorder occurs at $T \approx 1450$ K via the generation of vacancies in the topmost layer of the solid accompanied by the formation of an adlayer, a sharp drop in the structure factors and an increase in diffusion at the surface. We observed that the mechanism underlying this process involves initially the formation of divacancy-diadatom pairs. Further development of disorder and it's propagation upon increasing the temperature to the second and third layers of the solid occur via generation of vacancies adjacent to previously formed ones (in the same layer or in the layers above), accompanied by the formation of an adlayer, destabilization of the lattice structure, gradual loss of long-range order, and higher diffusion rates (of atoms and vacancies). The process culminates at $T \simeq 1700$ K in the formation of a quasiliquid surface region (extending over the adlayer and 2–3 layers of the original solid) characterized by interfacial liquidlike structural and atomic transport properties. In this context it is of interest to note that the approach to the quasiliquid state is characterized by a crystallographic anisotropy (enhanced loss of long-range order and larger diffusion rates along the $[1\bar{1}0]$ direction) and that at all temperatures prior to the melting of the material (at ~ 1733 K) the adlayer exhibits a larger degree of order than the adjacent layer underneath it.

From these observations we conclude that disordering of the Ni(110) surface region occurs first via anharmonic effects ($T < 1450$ K), the generation of top-layer vacancies accompanied by the formation of an adlayer at $T \simeq 1450$ K, the *gradual thickening* of the defective surface region (i.e., vacancy formation in deeper layers) at $T > 1450$ K, and the eventual formation of a quasiliquid surface region at $T \simeq 1700$ K. Above 1700 K the rate of loss of long-range order in the crystal and the increase in diffusion evolve (both in magnitude and spatially) in a "catastrophic" manner.

While the vacancy-driven mechanism of disordering found for Ni(110) is similar to that found in our previous study[50] of the (110) surface of aluminum, the temperature at which the Ni(110) surface premelts (formation of the quasiliquid layer) is much closer to the bulk melting temperature of the material, than that found for Al(110). This may be regarded as a reduced tendency of the (110) surface of nickel to premelt. Indeed application of the premelting condition in Eq. (1) to Ni(110) is consistent with the above observations.[2]

To further explore this issue, we present in this paper the results of MD simulation using the EAM interatomic interactions for Cu(110), which according to Eq. (1) should exhibit surface premelting.[2] Indeed, our results substantiate this expectation. Our results show the onset of defect formation in the topmost region of the crystal at $T \approx 900$ K, and a formation of a quasiliquid layer starting at ~ 1200 K, whose thickness increases logarithmically as the temperature approaches the melting point (determined in the simulations $T_m = 1284 \pm 10$ K), with a correlation length of 4.3 Å. These results show that in contrast to the (110) surface of nickel, the Cu(110) surface premelts at a temperature significantly lower (i.e., ~ 80 K) than the melting temperature of the bulk material.

The simulation method is described in Sec. II. The determination of the melting temperature of copper and the properties of the crystal-melt interface at coexistence are given in Sec. III. Results of simulations of the premelting process of the (110) surface of copper, and analysis motivated by Landau-Ginzburg (mean-field) theories of surface melting, are given in Sec. IV. We summarize our investigations in Sec. V.

II. METHOD

The embedded-atom method[59] (EAM) is a semiempirical method which provides a convenient framework for atomistic calculations of metallic systems. In this method the dominant contribution to the energy of the metal is viewed as the energy to embed an atom into the local electron density provided by the other atoms of the system, represented by an embedding energy function F which is supplemented by short-range, two-body interactions due to core-core repulsion, ϕ. The basic idea underlying this method is thus the same as that which motivated the development of the effective-medium theory[58] (EMT), and both find their roots in the density functional theory.[61] From the several parametrization procedures of the EAM which have been discussed,[59] we have chosen the one described by Foiles[60] in his study of liquid transition metals.

Since the MD simulation method which we have employed was described by us previously in the context of our studies of the crystal-melt and melt-vapor interfaces[52] and of the surface melting[51] of nickel we provide here only details pertinent to the present study.

In our molecular dynamics simulations the semi-infinite system is modeled via a thick slab of interacting dynamic particles which in addition interact with several

crystalline layers of a static substrate in the desired crystallographic orientation. Thus in these simulations periodic boundary conditions are imposed only in directions parallel to the surface plane. Because of the short range of the repulsive pair interactions and the finite range of the atomic charge densities it is sufficient to represent the static substrate by a small number of solid layers. The lattice constant of the static substrate, and thus the dimensions of the calculational cell in the direction parallel to the surface plane, is appropriate for the temperature of the simulation. From constant pressure[62] simulations of the bulk solid we determined that the lattice constant is adequately given by $a(T)=a(0)e^{\alpha T}$ where $\alpha=1.4\times10^{-5}$ K^{-1} (the experimental value at 300 K is $\alpha=1.66\times10^{-5}$ K^{-1}), and $a(T=0)=3.615$ Å.

In the first stage (Sec. III) we performed simulations aimed at determination of the melting temperature of bulk Cu. We start from a crystalline solid exposing a (111) surface, consisting of $N_L=21$ dynamic layers and 3 static substrate layers with $n_l=56$ particles in each layer, equilibrated at a high temperature of 1250 K [below the experimental melting point (1356 K) of the bulk solid[63]]. In this initial preparation stage a lattice constant of 3.679 Å, determined from a separate bulk simulation at 1250 K, was used, and the simulations were performed at constant temperature, using the canonical ensemble method[64] (i.e., stochastic thermalization of particle velocities). In all our simulations the particles' equations of motion were integrated using Gear's fifth-order predictor-corrector algorithm with a time step $\Delta t=5.15\times10^{-15}$ s. Further heating of the system (via stochastic collisions, or scaling of particle velocities) results in melting of the system starting from the free surface. We continue to adjust the energy content and lattice constant until about half of the (dynamic) system is molten. At this stage the system was allowed to evolve at constant energy for a prolonged period of time; 5×10^4 $\Delta t=257.5$ ps. The results which we present are time averages of the systems' properties performed over 2×10^4 $\Delta t=103$ ps, following the constant energy equilibration discussed above, with the system at the equilibrium coexistence state.

In the second stage of the study (Sec. IV) the properties of a semi-infinite crystal exposing the (110) surface were investigated at various temperatures. In most of our simulations ($T<1250$ K) the system consisted of 15 layers of dynamic particles with 70 atoms per layer, which in addition interact with five crystalline layers of a static substrate. Tests which we performed (see below) using a system consisting of 10 additional layers of dynamic particles, i.e., total of 25 dynamic layers, showed that while 15 layers are sufficient for $T\leq1250$ K, it is advisable to use the larger system at higher temperatures. Therefore for $T\geq1250$ K the results which we show were obtained by employing the 25-layer system in the simulations.

To study the properties at various temperatures, we equilibrate the system first at the desired temperature for at least 2×10^4 integration time steps, followed by an additional 2×10^4 time steps over which data are accumulated and averaged. Our simulations start from the low-temperature solid, and the system at each successively higher temperature is obtained starting from the equilibrated system at the temperature below it and adjusting the lattice constant to the new temperature.

Integration of the equations of motion yields the phase-space trajectories for the system from which physical properties and their time evolution can be obtained. To facilitate the presentation of our results, we define for any property g_i which depends on the phase-space point $(\mathbf{r}_i,\mathbf{v}_i)$ of atom i located at z_i (with $z=0$ set at the bottom of the dynamic slab and increasing toward the surface) a local density (per unit length) of that property at z by

$$\hat{\rho}_g(z)=\frac{1}{\sqrt{2\pi}\sigma}\sum_i g_i\exp\left[\frac{-(z-z_i)^2}{2\sigma^2}\right] . \tag{2a}$$

In our calculations a value about 10% of the layer spacing ($d_{110}=a/2\sqrt{2}$, $d_{111}=a/\sqrt{3}$) is used for the width parameter σ. This allows us to exhibit our results as continuous profiles in the z direction.

The particle number density (per length) profiles $\rho(z)$ are obtained by letting $g_i=1$ in Eq. (2). Other properties are presented as per particle local densities,

$$g(z)=\hat{\rho}_g(z)/\rho(z) . \tag{2b}$$

III. MELTING TEMPERATURE AND THE CRYSTAL-MELT INTERFACE

Results obtained via MD simulations, following the procedure described in Sec. II, are given in Figs. 1(a)–1(c) where we show, respectively, equilibrium (at crystal-melt coexistence) time-averaged profiles along the direction normal to the crystalline plane z for the particle density (ρ) and squared magnitude of the structure factor $|s_l(\mathbf{g})|^2$, potential energy (E_p), and of the layer diffusion coefficients obtained from

$$D_l=\lim_{t\to\infty}\frac{R_l^2(t)}{2n_d t} , \tag{3a}$$

$$D_{\parallel,l}=\lim_{t\to\infty}\frac{R_{\parallel,l}^2(t)}{4t}\quad (n_d=2) , \tag{3b}$$

$$D_{\perp,l}=\lim_{t\to\infty}\frac{R_{\perp,l}^2(t)}{2t}\quad (n_d=1) , \tag{3c}$$

where

$$R_l^2(t)=\left\langle\frac{1}{n_l}\sum_{i\in l}[\mathbf{R}_i(t+\tau)-\mathbf{R}_i(\tau)]^2\right\rangle , \tag{3d}$$

with the sum including atoms in layer l at time τ, the angular brackets indicate averaging over time origins (τ), n_d is the dimensionality, and $R_{\parallel,l}^2(t)$ and $R_{\perp,l}^2(t)$ are the components of $R_l^2(t)$ in the directions parallel and normal to the surface. Obviously the three-dimensional diffusion coefficient $D=2D_\parallel/3+D_\perp/3$. The structure factor [in Fig. 1(a)] is given by

$$S_l(\mathbf{g}_\alpha)=\frac{1}{n_l}\sum_{i\in l}e^{i\mathbf{g}_\alpha\cdot\mathbf{R}_i} ,\quad \alpha=1,2,3 , \tag{4}$$

where $\mathbf{g}_\alpha$ is the αth reciprocal lattice vectors. In Fig. 1(a)

the structure factor with $\mathbf{g}=(2\pi/a)[1\bar{1}0]$ is given.[65]

At coexistence (Fig. 1), the average temperature is uniform throughout the system (as is required in equilibrium) from which we determine the melting temperature $T_m = 1284K \pm 10$ K (the error estimate is an upper bond) in satisfactory agreement with the experimental[63] bulk melting temperature ($T_m = 1356$ K). From the profiles of the density [Fig. 1(a)] and the potential energy [Fig. 1(b)] we estimate the latent heat of melting as the difference between the average energies in the solid and liquid regions. The value thus obtained is 0.125 ± 0.005 eV/atom, compared to the experimental[63] value of 0.136 eV/atom.

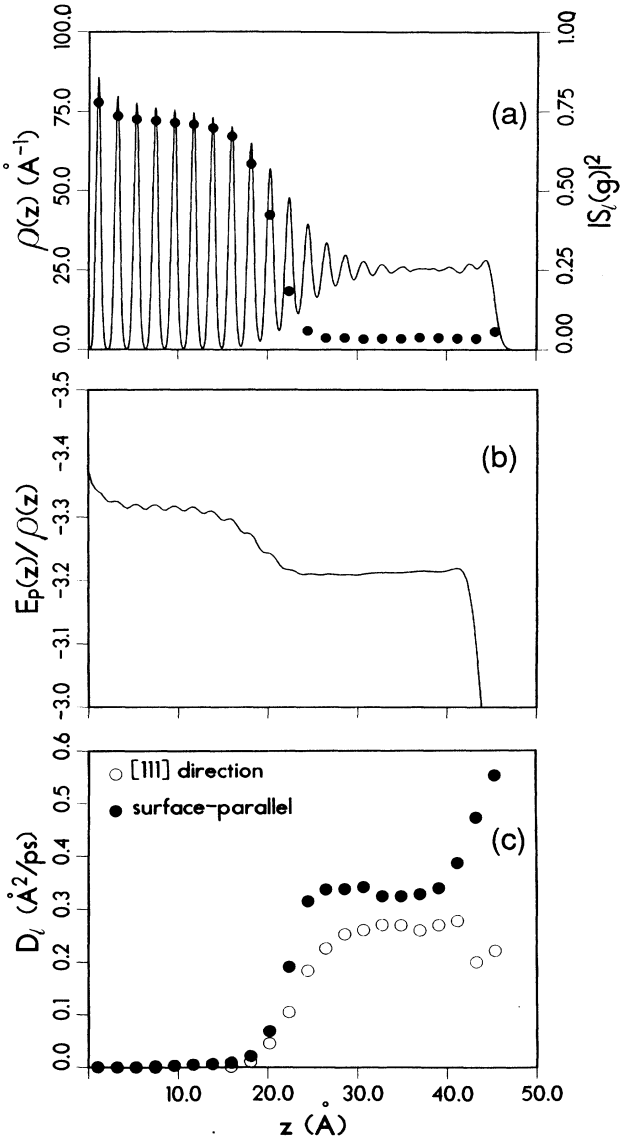

FIG. 1. Equilibrium profiles of the Cu(111) system at the melting point vs distance z, normal to the (111) plane, (a) density ρ (left) and structure factors (solid circles, right); (b) per-particle potential energy E_p; (c) diffusion coefficients in the directions normal (open circles) and parallel (filled circles) to the (111) surface plane. Energies and distances in units of eV and Å, respectively, and diffusion coefficients in units of Å^2/ps. Note the layered structure at the solid-melt interface and the increase in density in the melt-vapor interface.

Next we comment on properties of the crystal-melt interface at the coexisting temperature. Since the properties are similar to those of the Ni(111) crystal-melt interface the reader is referred to that study for details[52].

As seen from the density and energy profiles in Figs. 1(a) and 1(b), the systems exhibit two phases (a solid and a liquid) and two interphase interfaces (solid melt and melt vapor). The maxima in the density profiles [Fig. 1(a)] correspond to layer positions, which correspond to the minima in the energy profiles [Fig. 1(b)]. Furthermore, the solid-melt interface is diffuse exhibiting a gradual transition in properties from solid to the melt, portrayed both by the density and energy profiles, as well as by the structure factor [which may be taken as the order parameters, see Fig. 1(a)] and the diffusion coefficient profiles shown in Fig. 1(c). We note in particular that the diffusion in the direction normal to the surface plane is somewhat smaller than that in the parallel directions. The transition region between the solid and liquid regions extends over about 5–6 atomic layers. The transition interfacial region is stratified in the normal direction exhibiting "liquid layering," with the intralayer order decreasing for layers located further away from the crystalline surface (see further discussion in Sec. IV).

IV. SURFACE PREMELTING

To investigate the variation of the properties of the system with temperature we show first in Figs. 2 and 3 the density and total energy profiles of the system versus distance (z) normal to the surface plane, for various temperatures. From Fig. 2 (see also last column in Table I) we note (see in particular the lower temperatures) that the surface region is relaxed,[51,66] [i.e., $\Delta_{12} < 0$, where $\Delta_{12} = (d_{12} - d_{\text{bulk}})/d_{\text{bulk}}$]; d_{12} is the distance in the z direction between layers 1 and 2 of the crystal and $d_{\text{bulk}} = a/2\sqrt{2}$, where a is the lattice constant.[67] We observe a gradual change of the density profile with increase in temperature and the development of an "adlayer" (layer $l=0$) starting at a temperature as low as $T \approx 900$ K which is absent at low temperatures. The atoms in this layer originate from the underlying layers, as may be seen from Table I. We also note that the distinction between layers is blurred as the melting temperature is approached [see in particular Fig. 2(b)].

In order to verify that our calculations, performed mostly for a system of 15 layers of dynamic particles, provide a faithful simulation of the system (particularly at high temperatures) we show in Fig. 4 the density profiles (for the top 15 layers) obtained in two simulations at 1250 K, employing 15-layer (solid curve) and 25-layer (dashed curve) systems. It is evident that the two simulations yield rather similar results. However, deviations are observed, particularly for deeper layers. Consequently the larger system was used for $T \geq 1250$ K.

Similar characteristics to those shown in Fig. 2 are ex-

hibited in the per-particle total energy profiles versus z, shown in Fig. 3, where at each temperature the minima correspond to the layers' positions. In addition we include for comparison the energy profile for the liquid-to-vapor interface (dashed line) obtained from our previous simulations (see Sec. III) of the equilibrium liquid-to-crystal and liquid-to-vapor interfaces at coexistence. We observe that for all temperatures the energy of particles in the top region of the solid (layers 1 and 2) is higher than in deeper layers, due to the absence of particles on the vacuum side of the half-infinite solid. In addition we remark that already at $T=1275$ K the energy of particles in deep layers is close to that found in separate calculations for the bulk solid (-3.175 eV) and that of particles in the liquid region is close to the value for the melt (-3.05 eV) at the solid-to-melt coexistence point. Thus, the data shown in Figs. 2 and 3 indicate gradual formation of a liquid (or quasiliquid) film on top of the crystalline substrate. In particular we note that the energies of particles in the adlayer region are higher than in deeper regions, and that at the higher temperatures ($T \gtrsim 1200$ K) one may distinguish a liquid film region whose properties approach those of the bulk liquid. The interface between that liquid film and the underlying solid exhibits properties which are intermediate between those of the liquid and solid, as expected[52] (see Sec. III). Finally we note that throughout the process deeper layers in the system (e.g., $l \geq 8$ for $T < 1250$ K, i.e., the 15-layer system, and $l \geq 13$ for $T \geq 1250$ K, i.e., the 25-layer system) exhibit properties characteristic to the uniform bulk solid and thus we use the properties of these layers as reference bulk in analyzing the variations of the surface properties with increasing temperature (the influence of the static substrate may be seen for the 3–4 layers closest to it). Further evidence that for all $T \leq 1275$ K a region exhibiting bulk properties is maintained is provided by the structure factors to be discussed later and by the values of the spacings between solid layers that are in close agreement with the bulk values at the corresponding temperatures.

The structure of the system, and in particular the formation of the quasiliquid region can be analyzed using the layer pair-distribution functions, $p_l(r_\parallel)$, shown in

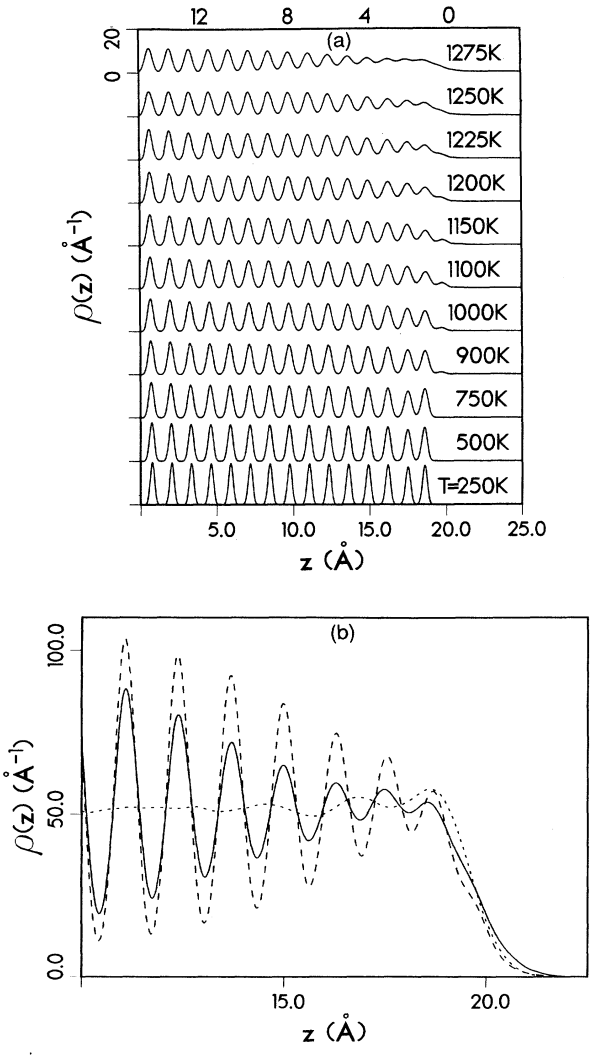

FIG. 2. (a) Equilibrium density profiles of the Cu(110) system vs distance z, normal to the surface plane for several temperatures. The layer's numbers are denoted on the top abscissa. Distance in Å, density in Å^{-1}. (b) Enlarged view of the density profiles in the surface region for $T \geq 1250$ K; long-dashed curve 1250 K; solid curve, 1275 K. In addition, the density profile near the surface of liquid copper at the triple point (1284 K) is shown, denoted by the short-dashed curve.

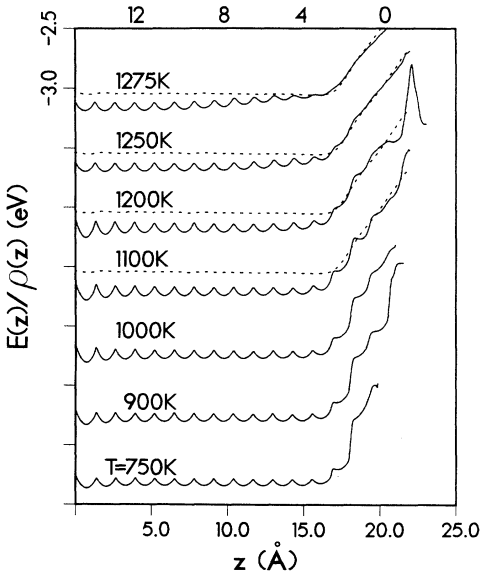

FIG. 3. Equilibrium total-energy per-particle profiles of the Cu(110) system, vs distance z, normal to the surface plane, for several temperatures. The minima correspond to layer positions. The layer's numbers are denoted on the top abscissa. Energy is in eV and distance in Å. The dotted curve corresponds to the energy profile of the surface of liquid Cu at the triple point.

TABLE I. Equilibrium averaged number of particles in the topmost layers of Cu(110) at various temperatures. The values at 1250 and 1275 K marked by an asterisk were obtained from simulations of 25-layer systems, all other values from simulations of 15-layer systems. The first surface layer of the crystal is $l=1$. Layer $l=0$ corresponds to the adatom layer that starts to form at 900 K. In the last column the percent of change in the spacing between layers 1 and 2, with reference to the bulk value, is given. The corresponding interlayer spacing relaxation at 0 K are $\Delta_{12}=-13.7\%$, $\Delta_{23}=0.02\%$. At 0 K the spacing between (110) layers is 1.2781 Å and at the coexistence point ($T_m=1284$ K) 1.3013 Å.

T (K)	0	1	2	3	4	5	Δ_{12} (%)
250	0.0±0.0	70.0±0.0	70.0±0.0	70.0±0.0	70.0±0.0	70.0±0.0	−14.0
500	0.0±0.0	70.0±0.1	70.0±0.1	70.0±0.1	70.0±0.1	70.0±0.1	−14.0
750	0.0±0.0	70.0±0.5	70.0±0.5	70.0±0.1	70.0±0.1	70.0±0.0	−13.0
900	6.1±0.7	64.2±1.1	69.7±0.4	70.0±0.4	70.0±0.1	70.0±0.0	−12.0
1000	9.5±1.3	60.1±1.6	69.9±1.3	69.9±0.7	70.0±0.4	70.0±0.1	−11.0
1100	16.1±1.9	54.6±2.4	69.8±1.7	69.6±1.1	70.0±0.7	70.0±0.1	−9.0
1150	20.1±2.9	50.7±2.9	19.7±2.0	69.7±1.4	69.8±1.0	70.0±0.2	−9.0
1200	13.7±3.2	58.4±4.0	69.2±2.5	69.4±1.9	69.5±1.3	70.0±0.2	
1225	17.6±3.8	57.2±3.5	68.5±3.0	69.1±2.2	69.3±1.7	69.5±0.6	
1250	18.8±4.1	60.1±4.9	66.0±3.6	68.0±3.1	68.2±2.3	69.3±1.9	
*1250	18.3±4.9	59.3±5.2	67.1±3.8	67.8±3.2	68.8±2.6	69.1±1.9	
*1275	27.9±5.9	62.1±6.2	64.5±4.4	65.1±4.1	67.6±3.8	66.9±3.3	

Figs. 5(a)–5(f) for $900\le T\le 1275$ K. The equilibrium $p_l(r_\parallel)$ functions are calculated as

$$p_l(r_\parallel)=\left\langle \frac{1}{n_l}\sum_{\substack{i,j\in l\\(i\neq j)}}\frac{1}{2\pi r_\parallel}\delta(r_{ij,\parallel}-r_\parallel)\right\rangle , \tag{5}$$

where $r_{ij,\parallel}$ is the component of $\mathbf{r}_i-\mathbf{r}_j$ parallel to the surface plane, n_l is the instantaneous number of particles in layer l, the sums extend over the particles in layer l, and the angular brackets denote averaging over time. For reference, the pair-distribution function for the bulk liquid at the melting point ($T=1284$ K) is shown (dotted line). As seen from Figs. 5(a)–5(f), the intralayer structure in the topmost layers of the system ($l\lesssim 3$) changes gradually from crystalline to liquidlike character as the temperature increases. We note that the topmost layer of the surface ($l=1$) is already liquidlike at $T\gtrsim 1200$ K. As we discussed before (see Refs. 51 and 52 and the references therein) the crystal-to-melt interfaces of metals, as well as other materials, are characterized by a "liquid-layered" transition region (or quasiliquid region), extending typically over several layers, wherein structural and transport properties of the material are influenced by the crystalline field of the underlying substrate, exhibiting a gradual transition from solid to liquid properties. We note that for the adlayer ($l=0$) at $T<1250$ K, the probability of finding particles with separations beyond the first-neighbor shell is small, indicating a tendency for clustering, which persists even for $T\approx 1250$ K [compare the ratio between peak heights in $p_l(r_\parallel)$ for $l=0$ and in the bulk].

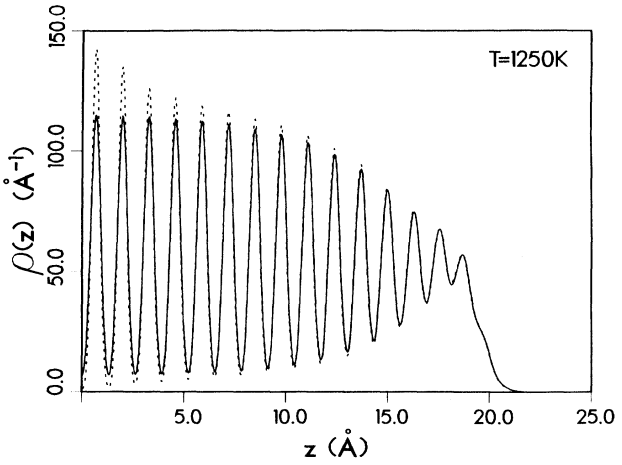

FIG. 4. Density profiles for Cu(110) at $T=1250$ K, obtained in simulations employing a system with 15 layers of dynamic particles (solid line) and 25 layers (dashed line). $\rho(\tau)$ in units of Å^{-1}, and distance in the direction normal to the surface plane in Å.

The observations discussed above are reflected and corroborated by the structure factors, see Eq. (4), calculated[67] for the three reciprocal lattice vectors: $\mathbf{g}_1=(2\pi/a)(2,\bar{2},0)$, along the atomic rows; $\mathbf{g}_2=(2\pi/a)(0,0,2)$, across the rows; and $\mathbf{g}_3=(2\pi/a)(2,2,0)$. As before n_l is the instantaneous number of particles in layer l, the sum extends over the particles in layer l.

The equilibrium averaged squared magnitude of the layer structure factors corresponding to the three reciprocal lattice vectors for the Cu(110) system equilibrated at selected temperatures are shown in Fig. 6. We note first that at low temperature [$T\le 1000$ K shown in Figs. 6(a) and 6(b)], the structure factors are constant throughout most of the system, exhibiting a decrease at the surface region. The deviation of $\langle |S_l(\mathbf{g}_\alpha)|^2\rangle$ from

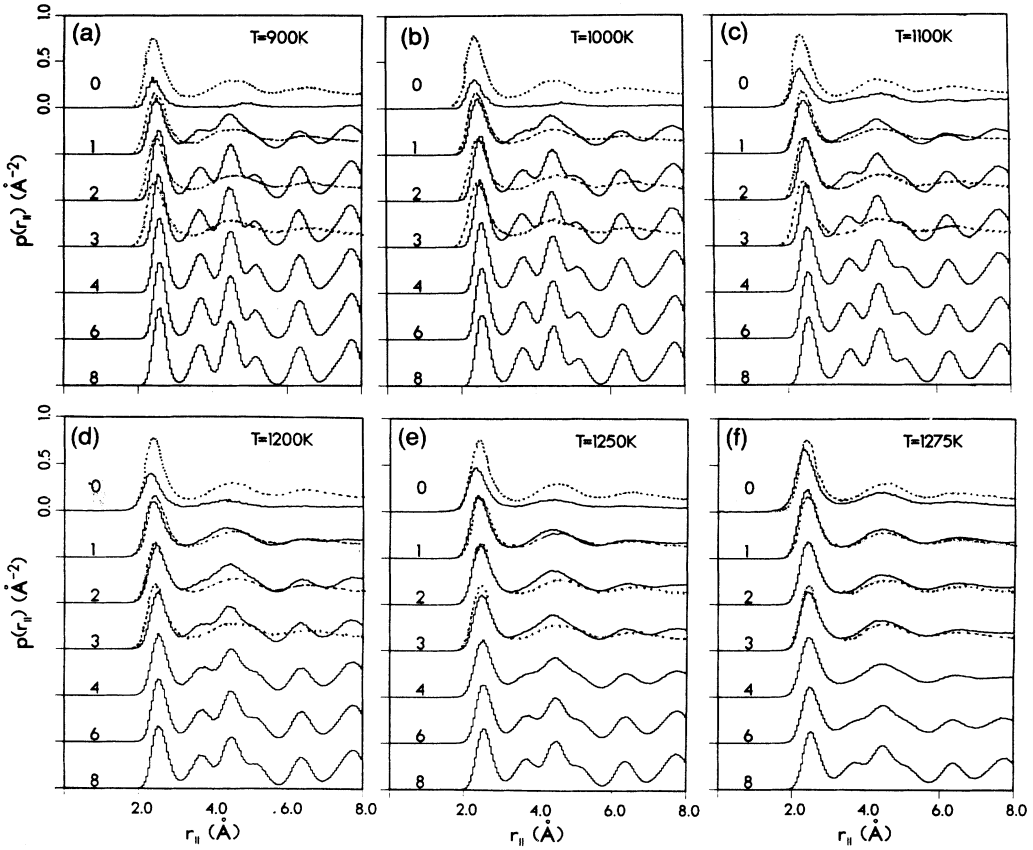

FIG. 5. Pair distribution functions, $p_l(r_{\|})$, in layers for the Cu(110) system equilibrated at several temperatures: (a) 900 K; (b) 1000 K; (c) 1100 K; (d) 1200 K; (e) 1250 K; and (f) 1275 K. Layer $l=0$ corresponds to the adlayer which forms at $T \gtrsim 900$ K. Note the gradual transition from solid to liquid character upon increasing temperature. The dashed line in (d)–(f) corresponds to the bulk liquid at the melting point. Distance in unit of Å.

unity originates from thermal vibrations and the decrease near the surface reflects the enhanced vibrational amplitudes of surface atoms. Note in particular the nonmonotonic behavior of $\langle |S_l(\mathbf{g}_3)|^2 \rangle$ near the surface [i.e., $\langle |S_1(\mathbf{g}_3)|^2 \rangle < \langle |S_2(\mathbf{g}_3)|^2 \rangle$ for $T < 1100$ K] which reflects a smaller root-mean-square (rms) vibrational amplitudes, in the direction normal to the (110), surface of the first-layer atoms than those of the second-layer atoms. Upon increasing the temperature the magnitudes of the structure factors decrease both in the bulk (due to enhanced vibrations) and in particular at the surface region (due to enhanced vibrations, generation of defects and disorder). In Figs. 6(b)–6(f) we observe that the structure factors for $\mathbf{g}_2$ (circles) and $\mathbf{g}_3$ (triangles) corresponding to the first layer are lower than those for the adlayer (layer $l=0$), indicating a higher degree of order in the latter. Apparently the adlayer atoms which for these temperatures originate mostly as a result of the generation of vacancies in the first crystalline atomic layer (see Table I) distort the structure of the underlying layer. This observation is corroborated by analysis of atomic configurations of the system and is similar to that observed previously[50,51] in simulations of the onset of disorder in the Al(110) and Ni(110) surface below the melting point.

As a check on the accuracy of the representation of the system, we show in Fig. 7 a comparison between the structure factors calculated from simulations at 1250 K, of a 15-layer and a 25-layer system. We note that even at this elevated temperature both simulations yield almost identical results in the topmost surface region of interest $l \leq 9$. However for $l \geq 9$ larger differences between the results of the two simulations are observed (i.e., compare the structure factors in layers $l \geq 9$). The three crystalline layers, $l=13$, 14, and 15 for the smaller system and $l=23$, 24, and 25 for the larger one, are influenced by the underlying static substrate. Therefore, as we already mentioned before (see Sec. II, and Fig. 4), the 25-layer system was used in simulations for $T \geq 1250$ K.

The structural data, presented as the natural logarithm of the squared magnitude of the layer structure factors corresponding to layers $0 \leq l \leq 5$ plotted versus temperature are shown in Fig. 8. The behavior of the structure factors versus temperature exhibits two regimes: (i) a low-temperature regime, $T \lesssim 1100$ K, characterized for all layers by a slow monotonic decrease of $\langle |S_l(\mathbf{g}_\alpha)|^2 \rangle$ upon increasing the temperature, and (ii) a high-

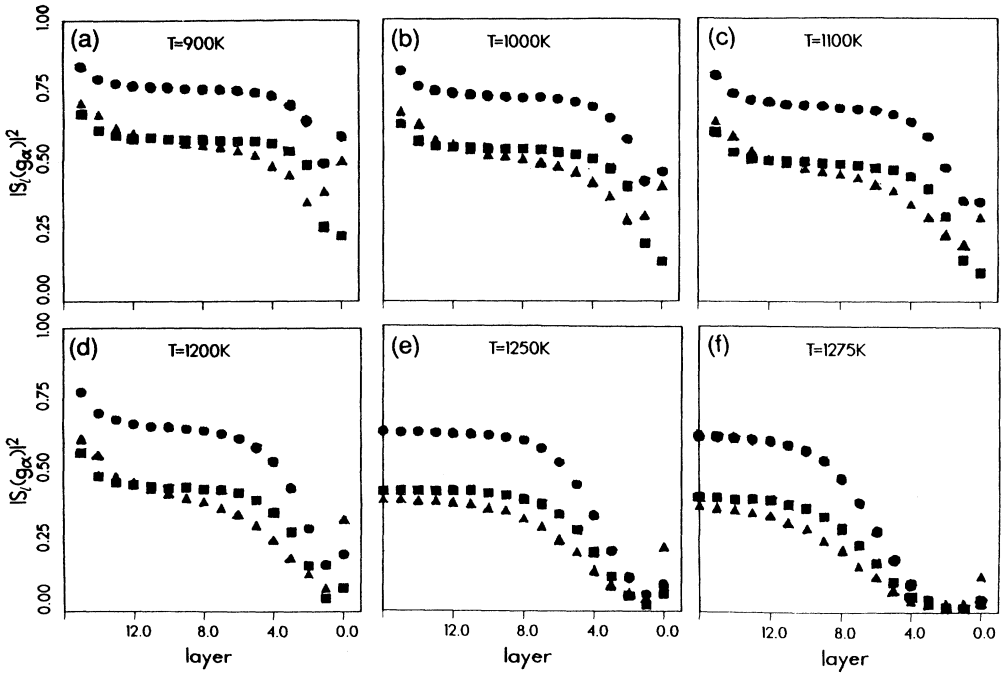

FIG. 6. Equilibrium averaged layer-structure factors squared $|S_l(\mathbf{g}_\alpha)|^2$, for $\alpha=1,2,3$ denoted by squares, circles, and triangles, respectively, vs layer number, at several temperatures: (a) 900 K; (b) 1000 K; (c) 1100 K; (d) 1200 K; (e) 1250 K; and (f) 1275 K. Note the lower magnitudes of the structure factors at the surface region and their decrease upon increasing temperature, with the onset of surface melting for $T \gtrsim 1200$ K. The higher values of $|S_0(\mathbf{g}_2)|^2$ and $|S_0(\mathbf{g}_3)|^2$ than those corresponding to the first layer ($l=1$) noted in (b)–(f) indicate a higher degree of order in the adlayer than in the first solid layer which distorts due to the creation of vacancies and the subsequent formation of the adlayer.

temperature regime, $T \gtrsim 1100$ K where the decrease of $\langle S_l(\mathbf{g}_\alpha)|^2\rangle$ with increase in temperature is more rapid for layers in the surface region of the material. In the harmonic approximation of solids (the Debye-Waller theory) $\ln\langle |S(\mathbf{g})|^2\rangle$ is proportional to T. For crystals deviations from linear dependence on temperature can be explained in terms of anharmonic vibrational effects. Considerations of these effects yield expressions[68–70] for $\ln\langle |S(\mathbf{g})|^2\rangle$ which contain in addition to the term linear in T, terms proportional to T^2 and T^3 and which can be used to fit the data. The coefficients of the quadratic and cubic terms depend on derivatives of the potential beyond the harmonic approximation and can be expressed within certain models in terms of characteristic material parameters, such as the Grüneisen and volume expansion coefficients.[70] Indeed the calculated data given in Figs. 8(a)–8(c) in the low-temperature region can be fit by such expressions.[71] For the surface region the behavior of the structure factors in the high-temperature regime cannot be fit by the above-mentioned expressions, reflecting the onset of defects and disorder [note also the appearance of vacancies and adatoms ($l=0$), at 900 K, evidenced in the data given in Table I].

The data given in Fig. 8 (and in Fig. 6) provide evidence for the anisotropy of properties at the (110) surface.[3,29,21,50] Comparing the data in Figs. 8(a)–8(c) corresponding to the surface region we observe that the structure factor for $\mathbf{g}_1$ [Fig. 8(a)] is the lowest (more negative) in both temperature regimes. This indicates a larger rms vibrational amplitude parallel to the surface plane along the atomic rows ($[1\bar{1}0]$ direction) and the persistence of long-range order across the atomic rows [Figs. 8(b)] to higher temperatures than that in other crystallographic directions. This conclusion correlates with our observa-

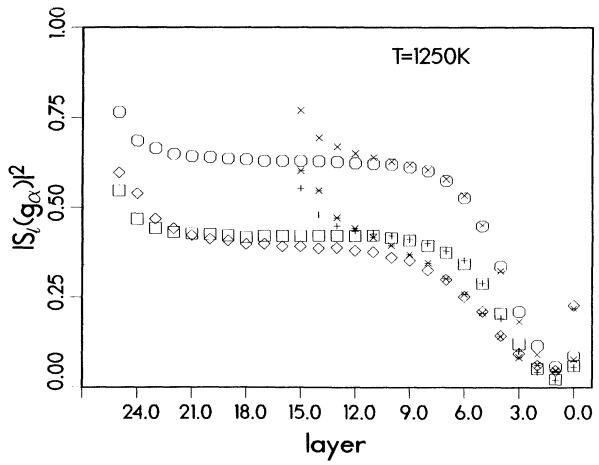

FIG. 7. Same as Fig. 6, at 1250 K, calculated from simulations of two systems of different sizes. The squares, circles, and diamonds correspond to structure factors $|S_l(\mathbf{g}_\alpha)|^2$, $\alpha=1,2,3$ calculated for a 25-layer system; +, ×, and * denote results obtained for a 15-layer system.

tions concerning enhance diffusion and tendency to disorder in the [1$\bar{1}$0] direction (see following discussion).

The melting transition of the top region of the solid is further shown by the layer diffusion coefficients, shown in Fig. 9 versus temperature, calculated from the particle trajectories generated in these simulations according to Eq. (3). The total diffusion coefficients ($n_d=3$) in the topmost layers of the system are shown in Fig. 9(a) and a decomposition ($n_d=1$) into diffusion coefficients along the atomic rows (in the [1$\bar{1}$0] direction) and across the rows (in the [001] direction) are shown in Figs. 9(b) and 9(c), respectively. As is evident from these results, the layer diffusion coefficients are larger for regions closer to

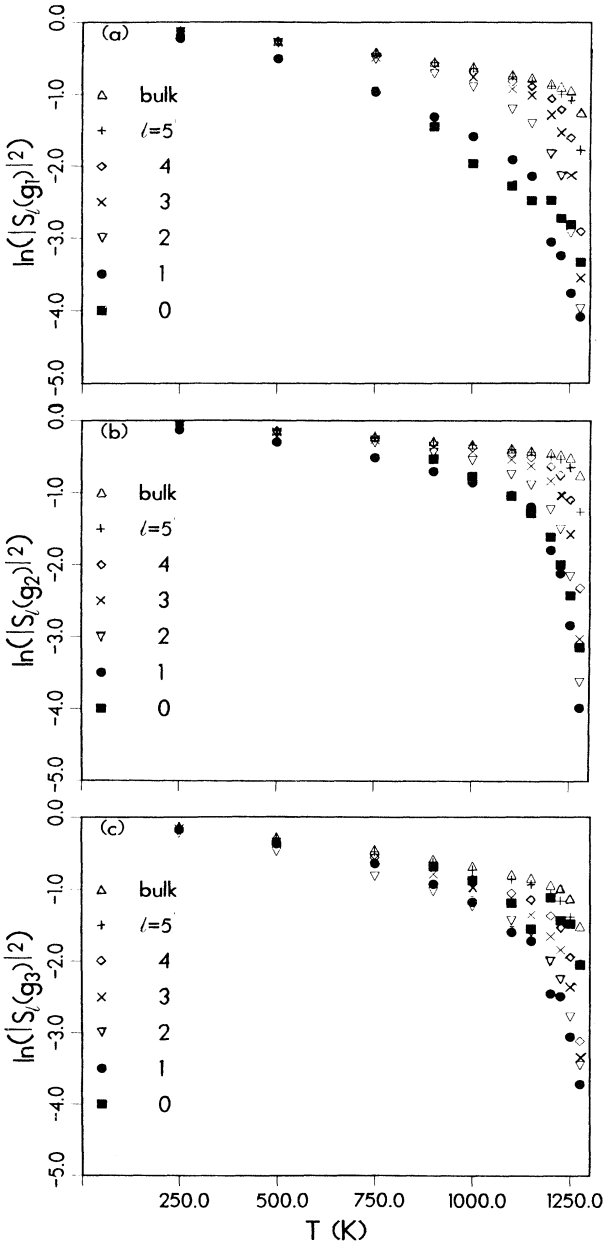

FIG. 8. Natural logarithm of the squared magnitude of the equilibrium averaged layer-structure factors, $|S_l(\mathbf{g}_\alpha)|^2$, for $\mathbf{g}_1$ (a) and $\mathbf{g}_2$ (b) and $\mathbf{g}_3$ (c) vs temperature. The symbols corresponding to the various layers are defined in the figure. Temperature in degrees Kelvin.

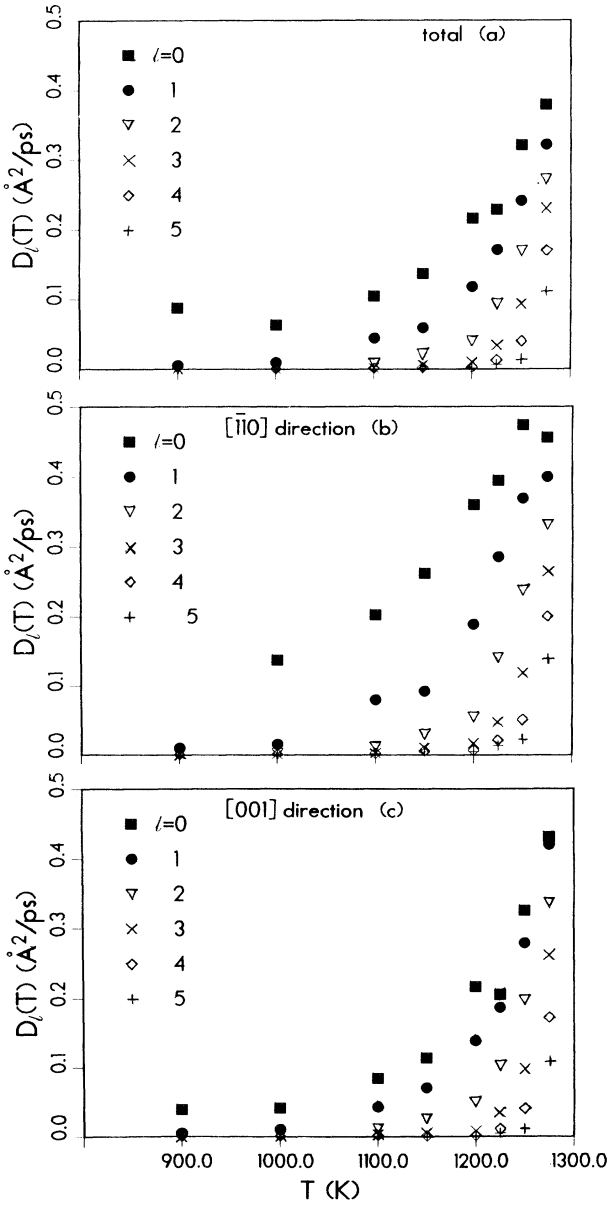

FIG. 9. Coefficients of diffusion in layers, vs temperature, for the Cu(110) system. Filled squares correspond to the adlayer, $l=0$; filled circles to the first layer; inverted triangles; $l=2$, $\times$'s denote the diffusion coefficients in layer 3, diamonds correspond to those in layer 4, and crosses for layer 5. (a) Total diffusion coefficients; (b) and (c) Diffusion coefficients along the atomic rows ([1$\bar{1}$0] direction) and across the rows ([001] direction), respectively. Note the marked increase in the rate of diffusion at $T \gtrsim 1200$ K (particularly for $l \leq 3$). Diffusion coefficients in units of (Å^2/ps) and temperature in degrees Kelvin.

the vacuum interface (i.e., $D_l > D_{l+1}$) exhibiting a slow gradual increase until $T \simeq 1200$ K, and a marked enhancement in the diffusion rates for $T \gtrsim 1200$ K (note that the onset of the increase of D_l for the fourth layer occurs at a somewhat more elevated temperature than that corresponding to layers $l \leq 3$). These observations correlate with the structural variations at the surface region exhibited in Figs. 6 and 8. Finally, we remark that the coefficients for diffusion along the rows ([1$\bar{1}$0] in Fig. 9(b)) are in general higher than those for the direction across the rows ([001] in Fig. 9(c)), which indicates an enhanced tendency for disordering and eventual initiation of melting in the former direction. These observations correlate with anisotropic diffusion on the (110) surface of Pb close to the bulk melting, measured via quasielastic scattering of low-energy He atoms,[29(b)] and with our results for the Ni(110) surface.[51]

We turn next to a quantitative discussion of the temperature dependence of the order parameters and thickness of the quasiliquid. As mentioned in the introductory section surface melting has been treated using the framework of Landau-Ginzburg (LG) theory[2,3,35–38] with single[2,3,35–38] and multicomponent[38] order parameters (OP). A natural choice of order parameters $m(\mathbf{g}_\alpha, z) \equiv m(\alpha, z)$ for our system are the magnitudes of the structure factors $|S(\mathbf{g}_\alpha, z)|^2$. Dividing the system into layers, as discussed above, and denoting the topmost layer of the crystal as $l = 1$, and the one next to the static substrate as $l = N_L$ we assume, in the spirit of the LG theory, the following form for the dependence of the order parameter on layer number [and thus distance along the normal to the (110) surface, increasing into the material],

$$m_l(\alpha) = \begin{cases} [m_b + (\tilde{m} - m_b)e^{-\beta(l-l^*)} + (m_{ss} - m_b)e^{-\beta_{ss}(l_{ss}-l)}], & l \geq l^* \quad (6a) \\ m^* e^{-\gamma(l^*-l)}, & l \leq l^*, \quad (6b) \end{cases}$$

where Eqs. (6a) and (6b) correspond to the solid and quasiliquid regions, respectively, and the model parameters depend on α, denoting the index of a reciprocal lattice vector g_α [we use in the following $\mathbf{g}_1$ and $\mathbf{g}_2$, which lie along and across the atomic rows in the (110) surface, respectively]. The parameters β and γ are the OP decay factors in the solid and liquid regions, respectively, and l^* and m^* are the location of the interface between the two regions and the value of the order parameter at the interface. m_b is the value of the OP in the bulk of the solid dynamical part of the system and $\tilde{m}$ is a fitting parameter of the model. The quantities l_{ss}, m_{ss}, and β_{ss} denote the layer location of the interface between the solid-static substrate and dynamic solid parts of the simulated system, an effective OP for that interface, and the decay constant into the dynamic solid, respectively. [The term in Eq. (6a) involving the static-substrate is included for technical reasons, and does not affect our results, see below.]

Requiring that the magnitude and slope of the OP's in Eqs. (6a) and (6b) will be equal at the interface between the solid and liquid (i.e., at l^*) yields

$$m^*(\alpha) = \tilde{m} + (m_{ss} - m_b)e^{-\beta(l_{ss}-l^*)}, \quad (7a)$$

and

$$\gamma = [\beta(m_{ss} - m_b)e^{-\beta(l_{ss}-l^*)} - \beta(\tilde{m} - m_b)]/m^*. \quad (7b)$$

In order to determine the various parameters of the model, we construct the function

$$F(m_b, \tilde{m}, \beta, l^*, m_{ss}, l_{ss}, \beta_{ss}) = \sum_{l=1}^{N_L} [m_l(\alpha) - |S_l(\mathbf{g}_\alpha)|^2]^2. \quad (8)$$

Using the layers' structure factors $|S_l(g_\alpha)|^2$, obtained from the simulations at different temperatures (see Figs. 6 and 8), the function F is minimized, via least-square fitting, with respect to it's arguments (in all cases the quality of the fit was such that $F/N_L \leq 2 \times 10^{-5}$). The values obtained by the fitting procedure were, for all cases, $m^* \simeq \tilde{m}$, $l_{ss} \simeq N_L + 1$, $0.8 \leq \beta_{ss} \leq 1.0$, $0.9 \leq m_{ss} \leq 1.0$, $\gamma \simeq 0.5$ for $T \geq 1250$ K, and $\gamma(\mathbf{g}_1) \approx 0.7$ and $\gamma(\mathbf{g}_2) \approx 0.3$ for lower temperatures. We also noted that the values of the other parameters, given in Table II, are not sensitive to small variations in the above parameters.

Motivated by the mean-field theoretical results,[3] we show in Fig. 10 the values obtained via the above fitting procedure for $l^*(T)$, the location of the solid-to-quasiliquid interface, plotted versus $-\ln(1 - T/T_m)$, where T_m is the calculated melting temperature ($T_m = 1284$ K), for two reciprocal lattice vectors in the (110) surface. As seen from the figure, for $T \geq 1225$ K, as well as for $T \leq 1000$ K, the results obtained for the two reciprocal lattice vectors nearly coincide. At the lowest temperatures ($T \leq 1000$ K) $l^* = 0$, increasing to a finite value for $T > 1000$ K. For $1000 \leq T < 1200$ K, $l^*(T) \simeq 1$. A straight-line fit to the data for $T \geq 1200$ K yields

$$l^*(T) = -\tfrac{5}{3}\ln(1 - T/T_m) - 3.33. \quad (9)$$

This expression can be converted to the quasiliquid thickness in units of length by multiplication with the layer spacing, for which we choose the value at the bulk at the melting point ($d = 1.3013$ Å at 1284 K), i.e., $z^*(T) = dl^*(T)$. Expressing $z^*(T)$ in the form

$$z^*(T) = -\frac{\xi_d}{2}\ln(1 - T/T_m) - z_0, \quad (10)$$

TABLE II. Values of parameters obtained by least-squares fitting [see Eqs. (6) and (8)], using values for the structure factors for two reciprocal lattice vectors ($\mathbf{g}_1$ and $\mathbf{g}_2$), obtained from simulations at various temperatures.

	$\mathbf{g}_1$				$\mathbf{g}_2$			
T (K)	m_b	m^*	l^*	β	m_b	m^*	l^*	β
1275	0.412	0.172	5.05	0.38	0.629	0.273	4.92	0.41
1250	0.423	0.182	2.77	0.49	0.633	0.308	2.81	0.51
1225	0.446	0.182	1.65	0.44	0.655	0.308	1.64	0.48
1200	0.444	0.144	0.90	0.57	0.657	0.331	0.24	0.53
1150	0.466	0.228	0.86	0.72	0.670	0.457	1.32	0.67
1100	0.493	0.218	0.45	0.67	0.692	0.487	1.07	0.68
1000	0.538	0.175	−0.10	0.84	0.729	0.425	0.00	0.69
900	0.576	0.271	0.00	1.2	0.757	0.497	0.00	0.80

lead to $\xi_d = 4.34$ Å ($\xi_d / d_{\mathrm{NN}} \simeq 1.7$, where d_{NN} is the nearest-neighbor distance at melting) for the correlation length in the solid. We note that our value for ξ_d is similar to that determined via mean-field analysis of the experimental results for Pb(110),[3,33] where $\xi_d = 6.3$ Å, and $\xi_d / d_{\mathrm{NN}} = 1.6$ for temperatures sufficiently below T_m so that short-range atomic interaction are dominant (regime I, see Refs. 3 and 33).

We should note that while z^* appears to obey the logarithmic dependence [Eq. (10)] predicted by the LG theory, ξ_d in Eq. (10) does not coincide with the correlation length d/β characterizing the decay of the order parameter in Eq. (6). In fact from Table II we observe that β varies with temperature, leading to values of $2.6 \lesssim d/\beta \lesssim 3.4$ Å for $T > 1200$ K where the logarithmic dependence of $z^*(T)$ on T is observed [see Eq. (10) and Fig. 10]. Furthermore, we note that the values for the correlation length (d/γ) of the OP in the quasiliquid (where $\gamma \simeq 0.5$ for $T \geq 1250$ K) is of similar magnitude (~ 2.6 Å) to that found in the solid.

Finally we discuss the mechanisms and energetics underlying the disordering leading to the nucleation of melting (in fact, gradual surface premelting) at the surface of the material. As shown in Table I and as noted in our discussion of the structure factors, the onset of disorder involves the generation of vacancies in the topmost layer ($l = 1$) of the crystal at ~ 900 K and the associated development of the adlayer ($l = 0$). We also note that at higher temperatures vacancies in deeper layers begin to appear. In this context we should emphasize the dynamic nature of the process as observed via analysis of particle trajectories revealing a host of intralayer and interlayer vacancy migration mechanisms. In Fig. 11 we plot the logarithm of the average number of adatoms ($l = 0$) and vacancies in the first layer versus $(k_B T)^{-1}$. The fact that the slopes of the adlayer and first-layer data are not

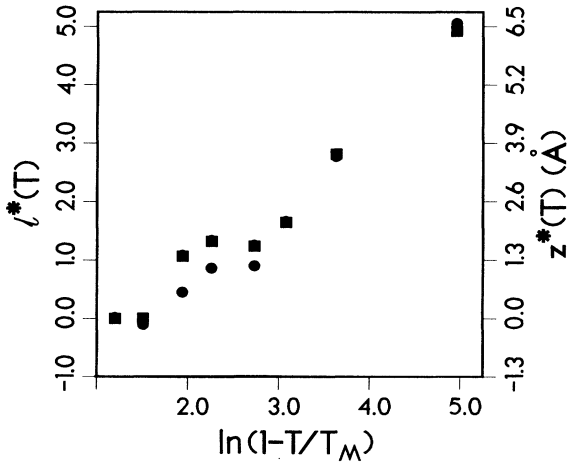

FIG. 10. The location of the solid-to-quasiliquid interface ($l^*(T)$, left scale; $z^*(T) = d l^*(T)$, right scale, where $d = 1.2013$ Å) vs $-\ln[1-(T/T_m)]$, where T_m is the melting point for Cu determined from our simulations. The values of $l^*(T)$ were obtained via the least-squares-fitting procedure as described in the text (see Table II). Filled squares and circles correspond to values obtained via the structure factors $\mathbf{g}_1$ and $\mathbf{g}_2$, respectively.

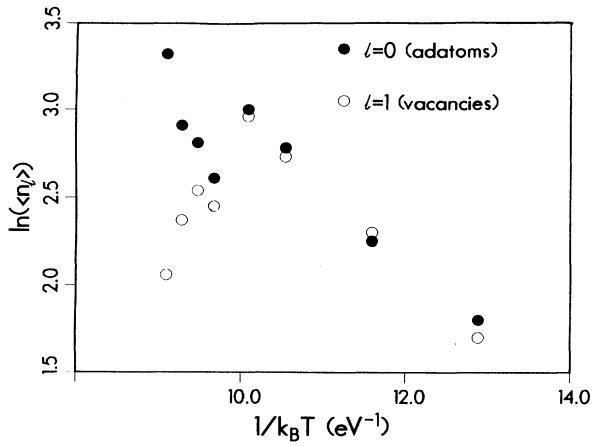

FIG. 11. Natural logarithm of the equilibrium average number of adatoms ($l = 0$, filled circles) and vacancies in the first layer ($l = 1$, empty circles) vs $(k_B T)^{-1}$ in units of eV. Note the linear relation for the lower temperatures $T \lesssim 1150$ K.

parallel to each other reflects the fact that at $T > 1150$ K not all the atoms in the adlayer ($l=0$) originate from the first layer ($l=1$). Using the slope of the data for $l=1$ in Fig. 11 up to 1150 K (above which premelting of the surface layer occurs) we estimate a vacancy-adatom-formation energy of ~ 0.4 eV. It is instructive to note that this value is much smaller than that (~ 1 eV) estimated in a similar manner in our investigation of the Ni(110) surface.

As we discussed in detail elsewhere[51] the vacancy-formation energy $E_{\rm VF}$ can be defined as

$$E_{\rm VF}=E(N-1,1)-E(N,0)-E_s \ , \tag{11}$$

where $E(N-1,1)$ is the energy of the solid containing $(N-1)$ atoms and a single vacancy $E(N,0)$ is the energy of the perfect solid, and E_s (>0) is the sublimation energy (negative of the cohesive energy per atom in the perfect infinite crystal) of the system. Similarly the adatom-formation energy $E_{\rm AF}$ can be defined as

$$E_{\rm AF}=\tilde{E}(N+1,1)-E(N,0)+E_s \ , \tag{12}$$

where $\tilde{E}(N+1,1)$ is the energy of the solid containing $(N+1)$ atoms, one of which is an adatom. It is difficult to obtain $E_{\rm VF}$ and $E_{\rm AF}$ at a specified finite temperature from the simulations because the small differences are obscured by the fluctuations in the total energy. Using a conjugate-gradient energy minimization (i.e., relaxation) in conjunction with the EAM potentials, we have determined first the zero-temperature values for the following quantities: $E_s=3.5366$ eV (compared to the experimental value[72(a)] of 3.54 eV); $E_{\rm AF}=0.217$ eV, and $E_{\rm VF}=1.127$ in the infinite bulk solid (compared to the experimental value[72(b)] of 1.3 eV). In this context we remark that in fitting the EAM potential parameters[60] only the bulk sublimation and vacancy-formation energies as well as bulk elastic constants have been used. Therefore, the values obtained for the energetics of the surface region of the material are consequences of the EAM potentials rather than fitted values. The cohesive energy of atoms in different layers, $E(l)$, given in Table III, is calculated for atom i in layer l from a decomposition of the EAM total cohesive energy expression to a sum of atomic contributions. This decomposition of $E_{\rm coh}$ is within the context of the parametrization of the EAM potentials[60] used by us, and in general is nonunique. Obviously, $E(l)$ is of smaller magnitude (less negative) for atoms in the surface layers, converging to $-E_s$ in deeper layers of the semi-infinite solid. The surface energy of Cu(110), $E_{\rm surf}$ can be obtained from the $E(l)$ values given in Table III as

$$E_{\rm surf}=\sum_l [E(l)-(-E_s)] \ , \tag{13}$$

yielding $E_{\rm surf}=0.7393$ eV/atom (i.e., 1350 erg/cm^2) compared to the measured[73] crystal-vapor surface energy (1790 erg/cm^2), which represents an average over several crystal faces, and to the value obtained by using a different parametrization of the EAM potentials[59(a)] (1400 erg/cm^2).

From Table III the single vacancy-formation energy [with and without relaxation, $E_{\rm VF}(l)$ and $E^0_{\rm VF}(l)$, respectively] is smaller in the topmost layer ($l=1$) and is largest in the second layer. We call attention to the anomalous behavior of the third layer, where we find that a vacancy in that layer is unstable and upon minimization of the energy of the semi-infinite crystal it migrates to the first layer [this is reflected in the large value of the relaxation energy, resulting in $E_{\rm VF}(3)=E_{\rm VF}(1)$]. Further discussion of vacancy-formation energies can be found in our earlier study.[51]

The smaller vacancy-formation energies which we find for the Cu(110) surface, in comparison to those calculated[51] for the Ni(110) surface, correlate with the enhanced premelting of the Cu(110) surface (i.e., formation of a quasiliquid layer), at a temperature (~ 1200 K) significantly below the bulk melting point $T_m=1284$ K, whereas the Ni(110) surface melts at a temperature ($T > 1700$ K) very close to T_m (1733 ± 30 K).

V. SUMMARY

In this paper we investigated the melting of the (110) surface of copper using molecular-dynamics simulations, in which the embedded-atom theory was used to describe the energetics and many-body interatomic interactions.

TABLE III. Energies in layers ($l=1$) is the topmost layer of the solid at $T=0$ K. $E(l)$ is the cohesive energy of atoms in layer l. $E^0_{\rm VF}(l)$ is the vacancy-formation energy without lattice relaxation [see Eq. (11)]. $E_{V,\rm relax}(l)$ is the relaxation energy following the vacancy formation. $E_{\rm VF}(l)=E^0_{\rm VF}(l)+E_{V,\rm relax}(l)$ is the vacancy-formation energy including lattice relaxation. $E_{\rm VF}(l)+E^{\infty}_{\rm af}$ [see Eqs. (11) and (12)] is the formation energy (including relaxation) of a vacancy adatom pair, with the adatom far from the vacancy. Energies are given in electron volts.

l	$E(l)$	$E^0_{\rm VF}(l)$	$E_{V,\rm relax}(l)$	$E_{\rm VF}(l)$	$E_{\rm VF}(l)+E^{\infty}_{\rm AF}$
1	−2.9432	0.276	−0.079	0.197	0.414
2	−3.4029	1.358	−0.084	1.274	1.491
3	−3.5232	1.291	−1.094	0.197	0.414
4	−3.5377	1.139	−0.017	1.122	1.339
5	−3.5368	1.141	−0.017	1.124	1.341
6	−3.5365	1.143	−0.016	1.127	1.344
bulk	−3.5366	1.143	−0.016	1.127	1.344

In addition, we determined that the bulk melting temperature for the model is 1284±10 K, and studied structural and transport (diffusion) properties of the solid-to-melt equilibrium interface at coexistence. As in the case of our previous study of nickel,[52] the solid-melt interface is diffuse, exhibiting a "liquid-layered" transition region (i.e., an interfacial region stratified in the normal direction to the plane of the crystal). Energetic and particle transport (diffusion) properties exhibit a gradual change from solid-to-melt behavior across the transition region (see Fig. 1).

The surface region of Cu(110) starts to disorder, via the generation of vacancies and formation of an adlayer at a temperature of about 900 K. At a temperature of about 1200 K (i.e., ~80 K below bulk melting) the onset of a quasiliquid region, which exhibits liquidlike energetic, structural, and transport properties, is observed.

Analysis of our results, motivated by Landau-Ginzburg (mean-field) theories, shows that the thickness of the quasiliquid layer $z^*(T)$ increases logarithmically as the temperature approaches the melting point, with a correlation length of 4.3 Å, in correspondence with results obtained via the analysis of experimental data[3,33] for Pb(110).

We also find, by fitting results for the structure factors obtained via the simulations to an assumed form of the dependence of the order parameter (OP) on distance from the solid-to-quasiliquid interface [see Eq. (6)], that the correlation length characterizing the decay of the OP in the solid takes values between 2.6 and 3.4 Å for $T > 1200$ K, where the logarithmic behavior of $z^*(T)$ with T is observed (see Fig. 10), and that the correlation length of the OP in the liquid for $T > 1250$ K is of similar magnitude (~2.6 Å).

Comparison of the results of this study to those obtained in our previous investigation of the melting of the (110) surface of nickel demonstrates the propensity of the Cu(110) surface to premelt with an onset well below the bulk melting temperature, while the Ni(110) surface melts at a temperature close to that of the bulk. These results are in agreement with those deduced for the two materials from a surface melting condition which relates the interfacial free energies of the solid, liquid, and vapor at coexistence.[2,3]

ACKNOWLEDGMENTS

This work was supported by U.S. Department of Energy (DOE) Grant No. FG05-86ER-45234. Calculations were performed at the Florida State University Computing Center and at the National Energy Research Supercomputer Center, Livermore, California, through computer-time grants by DOE.

[1]M. Faraday, Proc. R. Soc. London **10**, 440 (1860); in *Faraday Diary* (Bell, London, 1933), Vol. II, pp. 79–81; see also W. A. Weyl, J. Colloid Sci. **6**, 389 (1951).

[2]See review by J. van der Veen, B. Pluis, and A. W. Denier van der Gon, in *Chemistry and Physics of Solid Surfaces VII*, edited by R. Vanselow and R. F. Howe, Springer Series in Surface Science Vol. 10 (Springer-Verlag, Berlin, 1988), p. 455.

[3]J. F. van der Veen, B. Pluis, and A. W. Denier van der Gon, in *Kinetics of Ordering at Surfaces*, edited by M. G. Lagally (Plenum, New York, 1990), p. 343.

[4]J. G. Dash, in *Proceedings of the Solvay Conference on Surface Science: Austin, Texas*, 1987, edited by F. W. de Wette, Springer Series in Surface Science Vol. 14 (Springer-Verlag, New York, 1988), p. 142.

[5]G. Tammann, Z. Phys. Chem. **68**, 205 (1910); Z. Phys. **11**, 609 (1910).

[6]J. F. van der Veen and J. W. M. Frenken, Surf. Sci. **178**, 382 (1986), and references therein.

[7]D. Nenow, Prog. Cryst. Growth Charact. **9**, 1893 (1984), and references therein.

[8]J. W. M. Frenken and J. F. van der Veen, Phys. Rev. Lett. **54**, 134 (1985).

[9]J. W. M. Frenken, P. M. J. Maree, and J. F. van der Veen, Phys. Rev. B **34**, 7506 (1986).

[10]J. F. van der Veen, Surf. Sci. Rep. **5**, 199 (1985).

[11]Da-Ming Zhu and J. G. Dash, Phys. Rev. Lett. **57**, 2959 (1986).

[12]Da-Ming Zhu and J. G. Dash, Phys. Rev. Lett. **60**, 432 (1988).

[13]G. Fritsch, R. Lachner, H. Diletti, and E. Luscher, Philos. Mag. A **46**, 829 (1982).

[14]G. Fritsch, H. Diletti, and E. Luscher, Philos. Mag. A **50**, 545 (1984).

[15]R. H. Willens, A. Kornblit, L. R. Testardi, and S. Nakahara, Phys. Rev. B **25**, 290 (1982).

[16]J. L. Tallon, W. H. Robinson, and S. I. Smedley, J. Phys. Chem. **82**, 1277 (1978).

[17]D. Beaglehole and D. Nason, Surf. Sci. **96**, 357 (1980).

[18]Y. Furukawa, M. Yamato, and T. Kuroda, J. Cryst. Growth **82**, 665 (1987).

[19]E. G. McRae and R. A. Malic, Phys. Rev. Lett. **58**, 1437 (1987).

[20]P. von Blanckenhagen, W. Schommers, and V. Voegele, J. Vac. Sci. Technol. A **5**, 649 (1987).

[21]K. C. Prince, U. Breuer, and H. P. Bonzel, Phys. Rev. Lett. **60**, 1146 (1988).

[22]H.-N. Yang, T.-M. Lu, and G.-C. Wang, Phys. Rev. Lett. **63**, 1621 (1989).

[23]Y. Cao and E. H. Conrad, Phys. Rev. Lett. **64**, 447 (1990).

[24]G. Devaud and R. H. Willens, Phys. Rev. Lett. **57**, 2683 (1986).

[25]J. Krim, J. P. Coulomb, and J. Bouzidi, Phys. Rev. Lett. **58**, 583 (1987).

[26]A. Kouchi, Y. Furukawa, and T. Kuroda, J. Phys. C Suppl. **48**, 675 (1987).

[27]P. H. Fuoss, L. J. Norton, and S. Brennan, Phys. Rev. Lett. **60**, 2046 (1988).

[28]M. Bienfait, Europhys. Lett. **4**, 79 (1978).

[29](a) J. W. M. Frenken, J. P. Toennies, and Ch. Woll, Phys. Rev. Lett. **60**, 1727 (1988); (b) J. W. M. Frenken, B. J. Hinch, J. P. Toennies, and Ch. Woll, Phys. Rev. B **41**, 938 (1990); (c) J. W.

M. Frenken, J. P. Toennies, Ch. Woll, B. Pluis, A. W. Denier van der Gon, and J. F. van der Veen, in *The Structure of Surfaces II,* edited by J. F. van der Veen and M. A. Van Hove, Springer Series in Surface Sciences Vol. 11 (Springer-Verlag, Berlin, 1987).

[30]J. W. M. Frenken, J. Vac. Sci. Technol. **7**, 2147 (1989).

[31]K. D. Stock and E. Menzel, Surf. Sci. **61**, 272 (1976).

[32]K. D. Stock, Surf. Sci. **91**, 655 (1980).

[33]B. Pluis, T. N. Taylor, D. Frenkel, and J. F. van der Veen, Phys. Rev. B **40**, 1353 (1989).

[34]A. W. Denier van der Gon, R. J. Smith, J. M. Gay, D. J. O'Connor, and J. F. van der Veen, Surf. Sci. **227**, 143 (1990).

[35]R. Lipowsky, Phys. Rev. Lett. **49**, 1575 (1982).

[36]R. Lipowsky and W. Speth, Phys. Rev. B **28**, 3983 (1983).

[37]R. Lipowsky, Ferroelectrics **73**, 69 (1987).

[38]R. Lipowsky, U. Breuer, K. C. Prince, and H. P. Bonzel, Phys. Rev. Lett. **62**, 913 (1989); **64**, 2105 (1990); H. Lowen, *ibid.* **64**, 2104 (1990).

[39]W. K. Burton, N. Cabrera, and F. C. Frank, Philos. Trans. R. Soc. London **243**, 299 (1951).

[40]J. N. Stranski, Z. Phys. **119**, 22 (1942).

[41]J. Frenkel, *Kinetic Theory of Liquids* (Clarendon, London, 1946), pp. 425 and 426.

[42]J. K. Kristensen and R. M. J. Cotterill, Philos. Mag. **36**, 437 (1977).

[43]T. Kuroda and R. Lacmann, J. Cryst. Growth **56**, 189 (1982); D. Nenow and A. Trayanov, *ibid.* **79**, 801 (1986).

[44]F. A. Lindemann, Z. Phys. **14**, 609 (1910).

[45]L. Pietronero and E. Tosatti, Solid State Commun. **32**, 255 (1979).

[46]C. S. Jayanthi, E. Tosatti, A. Fasolino, and L. Pietronero, Surf. Sci. **152/153**, 155 (1985).

[47]C. S. Jayanthi, E. Tosatti, and L. Pietronero, Phys. Rev. B **31**, 3456 (1985).

[48]A. Trayanov and E. Tosatti, Phys. Rev. Lett. **59**, 2207 (1987); Phys. Rev. B **38**, 6961 (1988).

[49]G. An and M. Schick, Phys. Rev. B **39**, 9722 (1989).

[50](a) P. Stoltze, J. K. Norskov, and U. Landman, Phys. Rev. Lett. **61**, 440 (1988); (b) Surf. Sci. **220**, L693 (1989); P. Stoltze, J. Chem. Phys. **92**, 6306 (1990).

[51]E. T. Chen, R. N. Barnett, and U. Landman, Phys. Rev. B **41**, 439 (1990).

[52]E. T. Chen, R. N. Barnett, and U. Landman, Phys. Rev. B **40**, 924 (1989).

[53]J. Q. Broughton and G. H. Gilmer, Acta Metall. **31**, 845 (1983).

[54]J. Q. Broughton and G. H. Gilmer, J. Chem. Phys. **79**, 5095 (1983); **79**, 5105 (1983); **79**, 5119 (1983).

[55]V. Pontikis and P. Sindzingre, Phys. Scr. **19**, 375 (1987).

[56]V. Rosato, G. Cicotti, and V. Pontikis, Phys. Rev. B **33**, 1860 (1986).

[57]S. Valkealahti and R. M. Nieminen, Phys. Scr. **36**, 646 (1987).

[58]K. W. Jacobson, J. K. Norskov, and M. J. Puska, Phys. Rev. B **35**, 7423 (1987); J. K. Norskov, *ibid.* **26**, 2875 (1982).

[59](a) M. S. Daw and M. I. Baskes, Phys. Rev. B **29**, 6443 (1984); (b) S. M. Foiles, M. I. Baskes, and M. S. Daw, *ibid.* **33**, 7983 (1986).

[60]S. M. Foiles, Phys. Rev. B **32**, 3409 (1985).

[61]P. Hohenberg and W. Kohn, Phys. Rev. **136**, B864 (1964).

[62]M. Parrinello and A. Rahman, J. Appl. Phys. **52**, 7182 (1981).

[63]*Handbook of Chemistry and Physics,* edited by R. C. Weast (CRC, Cleveland, 1974).

[64]R. Fox and H. C. Anderson, J. Phys. Chem. **88**, 4019 (1984).

[65]The unit cell for the (111) system is defined by the primitive translation vectors: $\mathbf{a}_1=\frac{1}{2}\alpha(1/\sqrt{2},\frac{3}{2},0)$ $\mathbf{a}_2=\frac{1}{2}\alpha(-1/\sqrt{2},\frac{3}{2},0)$, and $\mathbf{a}_3=\frac{1}{2}a(1/\sqrt{2},1/\sqrt{6},2/\sqrt{3})$, where a is the lattice parameter (fcc cube edge length) obtained from a simulation of bulk solid Cu. $\mathbf{a}_1$ and $\mathbf{a}_2$ are parallel to the surface plane. The reciprocal lattice vectors are derived from the above as usual, i.e., $\mathbf{g}_i=2\pi(\mathbf{a}_j\times\mathbf{a}_k)/[\mathbf{a}_1\cdot(\mathbf{a}_2\times\mathbf{a}_3)]$, where (i,j,k) is the ordered triple (1,2,3) and its cyclic permutations.

[66]U. Landman, N. R. Hill, and M. Mostoller, Phys. Rev. B **21**, 448 (1980); R. N. Barnett, U. Landman, and C. L. Cleveland, *ibid.* **28**, 1685 (1983); R. N. Barnett, U. Landman, C. L. Cleveland, and R. H. Rast, J. Vac. Sci. Technol. **3**, (II), 1574 (1985).

[67]The two-dimensional unit cell in the (110) surface plane is defined by the unit vectors $\mathbf{a}_1=(a/2)(1,-1,0)$ and $\mathbf{a}_2=a(0,0,1)$ which lie along and across the atomic rows, respectively. The third direction is defined by the vector $\mathbf{a}_3=(a/2)(1,0,1)$. The spacing between atomic layers is $d=a/2\sqrt{2}$, and a is the fcc cube edge length for Cu. The dimensions of the calculational cell in the surface plane are $10\mathbf{a}_1$ and $7\mathbf{a}_2$, with 70 atoms/layer.

[68]A. A. Maradudin and P. A. Flinn, Phys. Rev. **129**, 2529 (1963).

[69]B. T .M. Willis, Acta. Crystallogr. Sec. A **25**, 277 (1969).

[70]J. Prakash and M. P. Hemkar, J. Phys. Soc. Jpn. **36**, 1608 (1974).

[71]R. N. Barnett and U. Landman (unpublished).

[72](a) *Metal Reference Book,* 5th ed., edited by C. J. Smith (Butterworths, London, 1976), p. 186; (b) R. W. Baluffi, J. Nucl. Mater. **69/70**, 240 (1978).

[73]W. R. Tyson, Can. Met. Quart. **14**, 307 (1975).